

CLUMP DEVELOPMENT BY THE NICKEL BUBBLE EFFECT IN SUPERNOVAE

to be published on ApJ 10 June 2005, v 626 1 issue

Chih-Yueh Wang

*Department of Physics
Chung-Yuan Christian University
Chungli, Taiwan 320*

ABSTRACT

We used one-dimensional radiative-transport radiation hydrodynamical simulations to investigate the formation of clumping in freely-expanding supernova ejecta due to the radioactive heating from the $^{56}\text{Ni} \rightarrow ^{56}\text{Co} \rightarrow ^{56}\text{Fe}$ decay sequence. The heating gives rise to an inflated Nickel bubble, which induces a forward shock that compresses the outer ambient gas into a shell. The radiative energy deposited by the radioactivity leaks out across the shock by radiative diffusion, and we investigate its effect on the evolution of the ejecta structure. Compared to the hydrodynamical adiabatic approximation with $\gamma = 4/3$, the preshock gas becomes accelerated by the radiation outflow. The shock is thus weakened and the shell becomes broader and less dense. The thickness of the shell takes up $\lesssim 4\%$ of the radius of the bubble, and the structure of the shell can be approximately described by a self-similar solution. We compared the properties of the shell components with those of the ejecta clumps indicated by our previous hydrodynamical simulations for the interaction of clumps with the outer supernova remnant. The high density contrast across the shell, $\chi \sim 100$, is compatible with that of ejecta clumps as indicated for Tycho's knots, but there is insufficient dense gas to cause a pronounced protrusion on the outline of a core collapse supernova remnant, like the bullets in the Vela remnant.

Subject headings: radiative transfer — supernova remnants — supernovae: general

1. INTRODUCTION

Observations of SN 1987A showed that the distribution of Fe in the ejecta is not what would be expected in the simplest models: it extended to higher velocity than expected and

had a large filling factor for its mass of $0.07 M_{\odot}$ determined from the supernova light curve (McCray 1993; Li, McCray, & Sunyaev 1993). A plausible mechanism for the large filling factor is the Ni bubble effect, in which the radioactive progenitors of the Fe expand relative to their surroundings because of the radioactive power deposition (Woosley 1988; Li et al. 1993; Basko 1994). This effect is important during the first ~ 10 days after the supernova, when the radioactive power is significant and the diffusion of energy is not yet an important process.

An expected effect of the Ni bubble expansion is to create clumps in the nonradioactive gas. There is widespread evidence that the ejecta of core collapse supernovae are clumpy. The oxygen line profiles in the nearby Type II supernovae SN 1987A (Stathakis et al. 1991) and SN 1993J (Spyromilio 1994; Matheson et al. 2000) showed evidence for structure, implying that the gas is clumped. The velocity range for the emission extends to $1,500 \text{ km s}^{-1}$ in SN 1987A and $4,000 \text{ km s}^{-1}$ in SN 1993J. Similar evidence for clumping has been found in the Type Ib supernova SN 1985F (Filippenko & Sargent 1989). Among young supernova remnants, Cas A is the prototype of the oxygen-rich SNRs, which show evidence for freely expanding, oxygen-rich ejecta in clumps. Puppis A, with an age $\sim 3,700 \text{ yr}$, is a more elderly example of such a remnant (Winkler et al. 1988).

Wang & Chevalier (2001, 2002, hereafter WC01, WC02) investigated the role of clumps in the evolution of supernova remnants. In Tycho’s remnant, believed to be the remnant of a Type Ia supernova, the presence of ejecta knots near the outer shock front requires a density contrast $\chi \gtrsim 100$ relative to the surrounding ejecta (WC01). The remarkable protrusions in the X-ray image of the Vela remnant are likely to be caused by ejecta clumps (Aschenbach et al. 1995) and WC02 found that $\chi \sim 1000$ is needed to create the structures. The free expansion velocities for the clumps were estimated at $\sim 3,000 \text{ km s}^{-1}$.

Our aim here is to investigate whether the Ni bubble effect can cause the clump structure apparently needed in the Tycho and Vela remnants. We compute one-dimensional hydrodynamical calculations, building on the work of Basko (1994), suitable for core collapse supernovae. We extend Basko’s work by including the effects of radiative diffusion and by carefully examining the density structure of the shell swept up by the Ni bubble. We further consider Type Ia supernovae using the same methodology. We show our computational setup and methods in § 2. The solutions for radiation-hydrodynamical effects are given in § 3. We also draw on the analogy to power input in a pulsar bubble to provide insight into the shell structure and evolution. In § 4 and § 5, we discuss the radiative effects on the Rayleigh-Taylor instabilities of the Ni bubble shell and the inferred ejecta-clump properties. Our conclusions are in § 6.

2. INITIAL CONDITIONS AND METHODS

We consider all of the ^{56}Ni synthesized in a supernova explosion initially resides in an isolated sphere in the center of supernova ejecta, with a mass M_{Ni} and a density contrast ω relative to the surrounding diffuse ejecta. The total radioactive energy released in the $^{56}\text{Ni} \rightarrow ^{56}\text{Co} \rightarrow ^{56}\text{Fe}$ decay sequence is deposited at a rate $q(t)$ (Basko 1994)

$$q(t) = \frac{Q_{Ni}}{t_{Ni}} \exp\left(-\frac{t}{t_{Ni}}\right) + \frac{Q_{Co}}{t_{Co}} \frac{\exp(-t/t_{Co}) - \exp(-t/t_{Ni})}{1 - t_{Ni}/t_{Co}}, \quad (1)$$

where t_{Ni}, t_{Co} and Q_{Ni}, Q_{Co} are, respectively, the mean life and specific decay energy of $^{56}\text{Ni}, ^{56}\text{Co}$:

$$\left\{ \begin{array}{l} t_{Ni} = 7.6 \times 10^5 \text{ sec} = 8.8 \text{ days}^\dagger \\ Q_{Ni} = 2.14 \text{ MeV/decay} = 3.69 \times 10^{16} \text{ ergs g}^{-1} \end{array} \right. \quad ^{56}\text{Ni} \rightarrow ^{56}\text{Co} \quad \left. \vphantom{\begin{array}{l} t_{Ni} \\ Q_{Ni} \end{array}} \right\}$$

$$\left\{ \begin{array}{l} t_{Co} = 9.64 \times 10^6 \text{ sec} = 111.5 \text{ days} \\ Q_{Co} = 4.57 \text{ MeV/decay} = 7.87 \times 10^{16} \text{ ergs g}^{-1}. \end{array} \right. \quad ^{56}\text{Co} \rightarrow ^{56}\text{Fe} \quad \left. \vphantom{\begin{array}{l} t_{Co} \\ Q_{Co} \end{array}} \right\}$$

(Lide 1992; † 8.5 days, Fireston & Shirley 1996). The accumulation of the total radioactive energy rises from 10^4 sec and saturates at $\gtrsim 10^7$ sec (about 25% of the total radiative energy is deposited between 10^7 and 10^8 sec, Fig. 1). Before the saturation point is reached, the radioactive energy can leak out of the bubble by radiative diffusion. This can occur while the gas remains optically thick to the ~ 1 MeV γ -rays.

We assume that the diffuse supernova ejecta are initially freely-expanding so that each gas element moves with a constant velocity $v = r/t$. The part of the ejecta unaffected by the radioactivity has its density drop as t^{-3} , and the pressure drops as t^{-4} for a $\gamma = 4/3$, radiation dominated fluid. We first refer our simulation initial conditions to Basko's parameters for SN 1987A (Basko 1994 and the references therein):

$$M_{Ni} = 0.075 M_{\odot}, \quad \omega = 3$$

$$t_0 = 10^4 \text{ sec}, \quad \rho_{a0} = 10^{-4} \text{ g cm}^{-3}, \quad P_0 = 2.5 \times 10^{11} \text{ dyn cm}^{-2},$$

where t_0 , ρ_{a0} and P_0 are the initial age, ejecta substrate density (surrounding the bubble), and background pressure, respectively. The initial velocity at the bubble edge $r = R_0$ is given by the initial ^{56}Ni density contrast and age:

$$U_0 = \frac{R_0}{t_0} = \left(\frac{3M_{Ni}}{4\pi\rho_{Ni}}\right)^{1/3} \frac{1}{t_0} = 7 \times 10^7 \omega^{-1/3} \text{ cm s}^{-1}.$$

For $\omega = 3$, $R_0 = 5.0 \times 10^{11}$ cm. The initial pressure is assumed uniformly distributed inside and outside the bubble, independent of the bubble size. The pressure in the Ni bubble is determined by the radioactive power input at later times.

We note that the above parameters give an ejecta structure comparable to the inner flat-density component of the power-law ejecta density model that has a power index $n = 8$ ($\rho \propto r^{-n}$ in the outer parts), an ejecta mass $M = 10 M_{\odot}$, and an explosion energy $E = 10^{51}$ ergs (Chevalier & Liang 1989). The transition between the flat and power law parts of the density profile occurs at $v = 3162 \text{ km s}^{-1}$ for these parameters. This set of explosion conditions is suitable for core collapse supernovae and had been used in our two-dimensional hydrodynamical simulations for the Vela supernova remnant (WC02). The energy density is initially dominated by the energy deposited by the supernova shock. Shigeyama & Nomoto's (1990, their Fig. 2) model for SN 1987A indicates an adiabat $\kappa = 6.3 \times 10^{15}$ (cgs units) where $P = \kappa \rho^{\gamma}$; for $t_0 = 10^4 \text{ sec}$, $\rho_0 = 9.4 \times 10^{-5} \text{ g cm}^{-3}$ in our density model, and so $P_0 = 2.7 \times 10^{10} \text{ dynes cm}^{-2}$. We take $P_0 = 2.7 \times 10^{10} \text{ dynes cm}^{-2}$ as the appropriate value at 10^4 sec . For $t_0 = 100 \text{ sec}$, $P_0 = 2.7 \times 10^{18} \text{ dynes cm}^{-2}$. The time to set up the free expansion phase depends on the radius of the star because of the effects of reverse shock waves. For a blue supergiant progenitor star, like that of SN 1987A, the timescale is $\sim 10^4 \text{ sec}$; for a red supergiant progenitor, the timescale is $\sim 10^5 \text{ sec}$. It is needed to initiate the simulations at $t \sim 10^2 \text{ sec}$ to acquire a numerically saturated solution at $t \gtrsim 10^4 \text{ sec}$ (the age of interest). The use of a freely-expanding velocity prior to this stage should not affect the 1-D symmetrical solution, considering that the radioactive heating is strong. Models of supernova explosions predict smooth ^{56}Ni profiles in both thermonuclear and core collapse supernovae, with the density contrast ω below a factor of 3 (Nomoto, Thielemann & Yokoi 1984; Woosley 1988). We vary ω in the range of $0.1 \leq \omega \leq 3$, with the other initial parameters scaled accordingly to the standard values described above.

Next we consider the initial parameters for Type Ia supernovae. We assume a powerlaw density profile $n = 8$ as in core collapse supernovae, with $M = 1.4 M_{\odot}$, $E = 10^{51}$ ergs, and $M_{\text{Ni}} = 0.5 M_{\odot}$. The transition between the flat and power law parts of the density profile occurs at $v = 8452 \text{ km s}^{-1}$ for these parameters. The background pressure in Type Ia ejecta is not well documented. To estimate, we make use of the entropy change $dS = dQ/T$ during the nuclear burning from C/O into Ni. During the process, $kT \sim 0.6 \text{ MeV}$, and the energy released per nucleon is

$$dQ \sim [2m(\text{C}) + 2m(\text{O}) - m(\text{Ni})] c^2 / 56 \sim 0.79 \text{ MeV/nucleon}, \quad (2)$$

where $m(\text{X})$ is the mass of element X; $m(\text{C}) = 12.0000 \text{ amu}$, $m(\text{O}) = 15.9949 \text{ amu}$, and $m(\text{Ni}) = 55.9421 \text{ amu}$ (Audi et al. 2003), and c is the speed of light. Then $dS \sim 1.3k / \text{nucleon} = 1.8 \times 10^{-16} \text{ erg/K/nucleon}$, where k is the Boltzmann constant (Shigeyama, private communication). The adiabat κ was obtained by relating the entropy per nucleon $S = [(4aT^3/3)(m(\text{Ni})/56)/\rho]$, where the initial entropy before the burning is ignored, to the

radiative pressure $P = aT^4/3$ and $P = \kappa\rho^{\frac{4}{3}}$. Substituting P and κ into S , we find

$$\kappa = \left[\left(\frac{3}{a}\right)^{1/4} \left(\frac{S}{4(m(\text{Ni})/56)}\right) \right]^{4/3} \sim 6.1 \times 10^{14} \text{ (cgs units)}. \quad (3)$$

For $t_0 = 10^4$ sec, $\rho_0 = 6.92 \times 10^{-7}$ g cm $^{-3}$ in our density model, and so $P_0 = 3.7 \times 10^6$ dynes cm $^{-2}$. The adiabat (and so the background pressure) could be higher, considering there is an initial entropy distribution that acts to freeze the deflagration front. The background energy density has the profile of the mass density because of the assumed uniformity.

We first approach the problem using hydrodynamical simulations with $\gamma = 4/3$ in both the bubble interior and the ejecta substrate. We follow the bubble-shell interface on a spherical expanding grid, and add the specific radioactive energy to the internal energy within the bubble uniformly and locally, i.e., in proportion to the local mass density. A reflecting condition is used for the inner boundary, and a non-zero gradient outflow condition is invoked on the outer boundary to eliminate the spurious shock raised by the grid expansion.

We further include radiation hydrodynamics (RHD) in the simulations using the ZEUS2D code (Stone, Mihalas, & Norman 1992). The radioactive power is deposited into the radiation instead of the material and $\gamma = 5/3$ for the matter. The code is based on finite difference and finite volume on an Eulerian grid and uses an artificial viscosity to smooth shock transitions. The RHD algorithm employs nonrelativistic full radiative transport, under the assumption of LTE (local thermal equilibrium) and gray opacity, and is thus equally applicable to both optically thin and thick media. The flow evolves towards the optically thin regime where radiation tends to stream away across the Ni bubble shell. The full transport scheme ensures the proper evolution while the radioactive energy is continually added within the bubble.

At the age of interest, the opacity is dominated by electron scattering. A maximum absorption 1/1000 times the magnitude of scattering is applied in our calculation. For completely ionized heavy elements, the Thompson scattering gives an opacity $0.2 \rho(r, t)$ cm $^{-1}$, where $\rho(r, t)$ is the material density. The initial energy is equally partitioned between radiation and material. Considering that a Type Ia has lower temperature and smaller radius, $P_{rad} \sim r^{-4}$ and $P_{gas} \sim r^{-5}$, the equi-partition assumption may be more valid for core collapse supernovae.

In the RHD algorithm, the coupled radiation and material energy densities are solved using Newton-Raphson iteration for convergence. When the radiation pressure is in excess of the gas pressure by several orders of magnitude, convergence becomes extremely difficult to reach. We thus stop the simulations prior to the optically thin stage. In our situation, the radiation effects are most important when the gas is still optically thick, so that the diffusion approximation is adequate. The choice of the flux limiters from which the Eddington tensor

is computed does not affect the diffusion result. For details of radiation hydrodynamics, we refer readers to Stone et al. (1992) and the references therein.

3. SHELL STRUCTURE AND EVOLUTION

3.1. Simulations

We show in Figs. 2, 3, and 4 the ejecta structure and evolution properties in the core collapse supernova model using $n = 8$, $E = 10^{51}$ erg s^{-1} , and $M = 10 M_{\odot}$. These simulations were initiated with $t_0 = 10^2$ sec, $M_{Ni} = 0.075 M_{\odot}$ and $\omega = 3$. The diffuse ejecta have an initial density $\rho_0 = 94.4$ g cm^{-3} and an accumulated radioactive energy density $e_{rad0} = 1.38 \times 10^{15}$ erg cm^{-3} . The initial material and radiation energy density in the background are equally divided, $e_0 = e_{r0} = 1.35 \times 10^{10}$ erg cm^{-3} .

We first examined the evolution of the flow in the purely hydrodynamic simulations. The expansion of the bubble gives rise to a strong forward shock behind which the ambient gas is compressed into a dense shell (Figs. 2 and 3). The inner edge of the shell is a contact discontinuity where the gas comoves with the bubble-shell interface; it has a high density because of the acceleration of the shell. The shock front is continually accelerated outward (Fig. 4(a)). To describe the acceleration, we use $a \equiv (dR_{sh}/dt)/(R_{sh}/t)$, the expansion rate evaluated at the shock front R_{sh} , equivalent to the velocity ratio of the shell to the preshock diffuse ejecta. We find that a rises to a maximum $\lesssim 1.20$ around $\lesssim 10^6$ sec, and subsequently tends to 1.0 at late times as the shell becomes comoving with the preshock gas (Fig. 4(b)). Because the background pressure has little influence on the dynamics, the shell structure becomes frozen into the flow.

The shell is very thin, with a thickness as a fraction of the radius $\beta \equiv h_{sh}/R_{sh} \lesssim 0.02$, where R_{sh} and h_{sh} are respectively the radius and thickness of the shell (Fig. 4(c)). The initial shock compression is set by the jump condition

$$\frac{\rho_1}{\rho_0} = \frac{(\gamma + 1)\mathcal{M}^2}{(\gamma - 1)\mathcal{M}^2 + 2}, \quad (4)$$

where

$$\mathcal{M} = \frac{v_{sh}}{c_0} = \left(\frac{dR_{sh}}{dt} - \frac{R_{sh}}{t} \right) \left(\frac{\rho_0}{\gamma p_0} \right)^{1/2} \quad (5)$$

is the Mach number of the shock, ρ_1 is the postshock density, v_{sh} is the shock velocity relative to the preshock gas, and c_0 is the sound speed in the preshock medium. For a radiation dominated, strong shock, $\rho_1/\rho_0 = 7$. The accelerating shell has a higher density in

the postshock region so that a typical compression factor in the shell (relative to the preshock gas) is $\chi \sim 10$ (Fig. 4(d)). The compression factor in the bubble is $\chi \sim 0.1$ (Fig. 4(e)). We note that $\beta \approx (3\chi)^{-1}$. The highest density occurs at the inner edge, where the density is limited by the numerical resolution (Fig. 3).

In the RHD case, the energy from the heated gas leaks out from the bubble energy reservoir as time progresses (Fig. 2). The gas is radiation dominated. Radiative diffusion allows the internal energy to propagate ahead of the shock wave, and so eliminates the temperature and the radiation pressure gradients. In order for diffusion to be dynamically important, it requires that the diffusion time scale, t_d , be smaller than the hydrodynamic time scale of the flow, t_h ; i.e.,

$$t_d \approx \frac{h_{sh}^2}{\lambda c} < t_h \approx \frac{h_{sh}}{v_{sh}} \quad (6)$$

where λ is the photon mean free path. We note that

$$\frac{t_d}{t_h} \approx \left(\frac{h_{sh}}{\lambda} \right) \left(\frac{v_{sh}}{c} \right). \quad (7)$$

At $t \approx 3 \times 10^6$ s, $h_{sh} = 10^{13}$ cm, $\lambda = 1/\kappa\rho = 5 \times 10^{10}$ cm, so that $t_d = h_{sh}^2/\lambda c = 6 \times 10^4$ s. At this time, $v_{sh} \approx 1 \times 10^7$ cm s⁻¹, so $t_d/t_h \approx 0.07$. The gas is optically thick, but radiative diffusion is important. As a result of diffusion, the preshock gas is accelerated by the radiation; the shock is then weakened. The shock front develops a radiative precursor (Fig. 2). The acceleration of the bubble shell is reduced because of the radiative loss. The rise in the preshock sound speed and the acceleration of gas ahead of the shock reduced the shock compression (eqn. [4]). The shell becomes broader and less dense compared to the HD case (Fig. 4(c)). The sharp density jump at the shock front in the RHD case is also smoothed out before the gradient of e_r diminishes to zero (Fig. 4(d)). The gas tends toward a freely expanding state in which the density profile is frozen into the flow.

The diffusion effect speeds up the freeze-out of the ejecta structure. For our parameters, the freezing occurs at a velocity $v_f \sim 1500$ km s⁻¹ and a time $t_f \sim 10^7$ s, significantly earlier than the HD case where $t_f \sim 10^9$ s and $v_f \sim 1900$ km s⁻¹ (Fig. 4(f)). In the HD case, the expansion sustains until pressure equilibrium is reached. Both cases show a density contrast $\chi \gtrsim 10$ between the shell and the preshock ejecta. The inner edge (contact discontinuity) of the shell is the densest with $\chi \gtrsim 100$. The shell thickness is increased to $\sim 4\%$ of the radius of the bubble. The swept-up mass in the shell remains about $M_s \sim 1 M_\odot$ (Fig. 4(g)). Note that we define the thickness as the distance from the contact discontinuity to the postshock outer dense region at the shock front, considering that the outermost postshock density profile flattens out into the ejecta substrate. At $\lesssim 10^7$ sec, the surface density of the shell drops below $\sim 17 - 33$ g/cm², the mean free path for the ~ 1 MeV γ -ray photons (Woosley,

Pinto, & Hartmann 1989; Shigeyama & Nomoto 1990). We stopped the RHD calculations prior to this time (Fig. 4(h)). When the initial Nickel mass is increased to 3 times $0.075 M_{\odot}$, the onset of freezing delays to $t_f \sim 10^8$ s with $v_f \sim 1800$ km s $^{-1}$ and $M_s \lesssim 3 M_{\odot}$. For a 10 times increase, $t_f \sim 10^8$ s, $v_f \sim 2400$ km s $^{-1}$, and $M_s \sim 5 M_{\odot}$ (Fig. 5). It is therefore expected that the radiation relaxes before 10^8 s, given any large Ni overabundance. The reason is that the photon mean free path is increased by the broadening of the shell, and so diffusion becomes more rapid with time.

3.2. Effect of Radiation

The effect of radiative diffusion does not increase the density contrast of the Nickel bubble shell, as in shell formation during shock break-out in a Type II supernova where radiative energy losses by diffusion lead to a large compression that is eventually limited by the gas pressure (WC01, Chevalier 1976). In the latter case, the flow behind the shock wave is being decelerated, and the immediate postshock region is being compressed. A drop in the dominant radiation pressure then is compensated by compression of the gas to the point where gas pressure becomes important, resulting in a large density enhancement. In our case, the pressure gradient has an opposite sign; the pressure decreases outward from the contact discontinuity to the shock front, and the radiative loss to the preshock gas is replenished by the energy diffusing from the bubble. The diffusion of energy ahead of the shock front leads to a weaker shock front and less compression in the shell.

3.3. Models for Type Ia supernovae

We investigated the ejecta structure for Type Ia SNe using the inner flat component of the power law model, $n = 8$, $E = 10^{51}$ ergs, and $M = 1.4 M_{\odot}$. We present the evolution of the dynamical properties in Fig. 7. The simulations were our highest resolved runs initiated with $t_0 = 10^2$, $M_{Ni} = 0.5 M_{\odot}$, and $\omega = 1.5$. The initiated time gives an initial mass density $\rho_0 = 6.92 \times 10^{-1}$ g cm $^{-3}$, and an initial material and radiation energy density $e_0 = e_{r0} = 5.5 \times 10^{14}$ erg cm $^{-3}$ for a standard adiabat $\kappa = 6.1 \times 10^{14}$ (cgs units). Here a lower background pressure was used, $e_0 = 1.3 \times 10^{13}$ erg cm $^{-3}$. The initial ^{56}Ni has an accumulated radioactive energy density $e_{rad0} = 3.15 \times 10^9$ erg cm $^{-3}$.

The evolution of the flow is similar to the case of core collapse supernovae. The Nickel bubble shell has a density increase toward the contact discontinuity, with the density contrast reaching $\chi \sim 100$. The diffusion effect speeds up the freeze-out of the ejecta structure. A

notable difference in the shell is that it is thinner, with a very prominent precursor (Fig. 6). Compared to core collapse supernovae, the ejecta has a higher ratio of background energy to mass ($\propto E/M$), thus the acceleration of the bubble is weaker. The expansion rate a rises to a maximum 1.04 before radiation relaxes, barely faster than the free expansion. The thickness of the shell reaches $\beta \sim 0.004$ at the turnover. The freezing occurs at a velocity $v_f \sim 7000 \text{ km s}^{-1}$ and a time $t_f \sim 10^7 \text{ s}$. The gas becomes optically thin at $\sim 10^6 \text{ sec}$. By this time, the RHD results do not diverge substantially from the HD results, but the velocity and the accumulated mass curves had started to flatten out, indicating that the radiation effect becomes dynamically less important.

We note that the swept-up mass in the RHD case may be underestimated due to the large precursor; we expect $M_s \sim 0.5 M_\odot$ as in the HD case. For a less amount of ^{56}Ni , we found that $M_s < 0.3 M_\odot$ and $v_f \sim 5500 \text{ km s}^{-1}$ for $M_{\text{Ni}} = 0.225 M_\odot$, and $M_s < 0.2 M_\odot$ and $v_f \lesssim 4000 \text{ km s}^{-1}$ for $M_{\text{Ni}} = 0.075 M_\odot$ (Fig. 5).

3.4. Variation of the Initial Parameters

We carried out simulations with a variety of initial conditions. We found the solution in the saturated regime is insensitive to the initial background pressure in the ejecta (Fig. 8). In the case of a higher initial background pressure that exceeds the accumulated radioactive pressure, the sharp structure in the shell takes more time to build up (for which grid resolution also has an effect), but the solution gradually converges once the radioactive energy input becomes dominant. E.g., the case using a smaller background pressure $P_0 = 2.7 \times 10^{10} \text{ dyn cm}^{-2}$ is no different from the standard case using $P_0 = 2.7 \times 10^{18} \text{ dyn cm}^{-2}$ (for the core collapse SN model with $t_0 = 10^2 \text{ sec}$), except that the former shows a more pronounced postshock oscillation trailing in the bubble. Likewise, the solution in our Type Ia model appears insensitive to the variation of background pressure. Our case using the standard κ shows little differences from the case in Fig. 7. We expect that the insensitivity would sustain with a higher value of κ . Simulations initialized before 10^4 sec allow the flow to saturate before the age of interest, and so the results are also insensitive to the initial distribution of energy between radiation and material, absorption rate, and details of radiative transport.

We also varied the initial ^{56}Ni density contrast. We assumed ^{56}Ni initially in pressure equilibrium with the ambient ejecta, so that its initial background energy increases with decreasing ω . Thus for $\omega = 0.1$ the shell expands to an outer radius. However, the change from $\omega = 3$ to $\omega = 1$ does not alter the shell properties we determined (Fig. 8).

4. ANALOGY TO PULSAR WIND NEBULAE

Chevalier (1984) has considered a constant-luminosity pulsar bubble interacting with constant density, freely-expanding supernova ejecta. We compare his self-similar solution with our hydrodynamical case, since the time evolution of the driving power is the only difference. The self-similarity exists for a power-law ejecta density $\rho \propto v^{-n}t^{-3}$ and a time-varying pulsar luminosity $L \propto t^{-l}$, when $n \lesssim 3$ and $l \lesssim 1$ (Jun 1998); the expansion law is $r \propto t^{(6-n-l)/(5-n)}$, as obtained from dimensional analysis. For a constant luminosity $l = 0$ and flat ejecta $n = 0$, $r \propto t^{1.2}$. The shock cannot be slowed down in the ejecta more than the free expansion rate, so the self-similar solutions only exist for $a \gtrsim 1$, i.e. $l \lesssim 1$.

In our solutions, the shell starts to accelerate with $a \gtrsim 1$. The evolution of the density profile can thus be compared to the self-similar solutions with varying l . In the self-similar solutions, decreasing l (i.e. increasing power input), or increasing the expansion rate, increases the shell thickness. For $l = 0$ and $a = 1.2$, we have $\beta = 0.02$. The shell thickness in our simulations shows a more complicated evolution than indicated by the measured expansion rate; the maximum expansion rate measured occurs at 6×10^5 sec, while the maximum thickness occurs at 5×10^6 sec. The first turnover in the thickness evolution seems to correlate with the change in the luminosity power index (see Fig. 9) at 5×10^6 sec; the second turnover occurs after 10^7 sec when the self-similarity breaks down because $l > 1$.

We overplot our solution at 4×10^5 sec on the self-similar solution with $l = 0.03$ in Fig. 10. The density distribution in the shell shows a sharp inward increase towards the contact discontinuity, with over 80% of the shell mass concentrated within the inner 50% region in radius (Fig. 11). The self-similar density is infinite at the contact discontinuity. The coarseness of the grid obviously sets limits on the highest density computed in the grid domain. Our results show a higher density contrast on fixed grids, because the numerical noise is smaller than on expanding grids. The shell can be distorted by instabilities (Basko 1994; Jun 1998), but we expect the density contrast to remain comparable.

Basko’s (1994, his Fig. 1) HD solutions suggest that the density contrast of the shell is only $\chi \sim 5$ at 4×10^5 sec. We reproduced his case and found that the shell broadens to $\beta > 0.1$ at $\sim 4 \times 10^4$ s, the turnover is much earlier than in our calculation using $t_0 = 10^2$ s. In his case using $t_0 = 10^4$ s, the radioactive energy accumulated to 10^4 s was deposited all at one time in the beginning of the calculation, so an excessive acceleration and a large broadening of the shell were the result. Basko’s Fig. 6 for the shell surface density has the same earlier turnover, suggesting this heating effect.

We note that the shell characteristics such as the density contrast and the thickness ratio should only be weakly dependent on the initial ^{56}Ni mass, since these properties can

be approximated by the self-similar solutions.

The deformation of the bubble-shell interface due to the Rayleigh-Taylor instability is likely to have a morphology similar to that of the pulsar bubble shell studied by Jun (1998) in two-dimensional simulations. The main difference is that magnetic fields constrain the instability in the pulsar bubble case, but are unlikely to be important for our case. The Rayleigh-Taylor spikes are directed inward, because of the shell acceleration. However, the instability should eventually end when the shell stops accelerating in the comoving stage. The effect of radiation diffusion is to smooth the pressure gradients, which ends the shell acceleration and the instability growth. The Jun (1998) simulations indicate that the instability does not cause radioactive material to have a significantly higher final velocity (see also Basko 1994).

5. NICKEL BUBBLE SHELL AS EJECTA CLUMPS

We now compare the properties of the Ni bubble shell with the initial properties of the clumps/bullets inferred from our previous clump-remnant simulations for Tycho’s remnant and the Vela supernova remnant. We consider that the ejecta clumps originate as components from the breakup of the shell, and examine if the inferred clumps (shell fragments) are able to survive the crushing in the remnant. The robustness of the clumps can be determined by three parameters: the initial density contrast, χ , between the clump and supernova ejecta; the initial impact time with the reverse shock, related to the initial ejection velocity; and the initial size of the clump. The high density contrast created across the shell, $\chi \sim 100$, is compatible with that of ejecta clumps needed to survive crushing in the remnant. In our model for the Vela remnant ($M = 10 M_{\odot}$, $E_{51} = 1$, and $M_{Ni} = 0.075 M_{\odot}$), the shell’s frozen-in velocity, $v_f \sim 1500 \text{ km s}^{-1}$, is within the range $1000 \lesssim v \lesssim 3000 - 4000 \text{ km s}^{-1}$ we determined as the most likely origin for the Vela bullets (WC02). If the shell has not been greatly disturbed, the clumps should be present in bands at the restricted velocity space; they are expected to enter the remnant’s intershock region at a normalized time $t' \sim 2.2$, or $\sim 2800 \text{ yrs}$ (see Fig. 1 in WC02 and Fig. 12). The velocity-restricted nature may have been detected in the wavelike clumpy structure immediately below Tycho’s blast wave front (Reynoso et al. 1999, WC01). If the clumps attain a size about the thickness of the shell, $\beta = 0.04$, then at the time of the initial reverse shock impact, the clumps have an initial size $a_0 \sim 8\%$ in terms of the intershock width, or $r_0 \lesssim 3\%$ in terms of the forward shock radius (Fig. 1 in WC02). Compared to the late clump-remnant interaction in WC02 that used a larger clump size $a_0 \sim 1/3$, the inferred clumps do not appear to have a sufficient strength to cause a protrusion on the forward shock. Nevertheless, since the computed highest density

is limited by numerical resolution, a larger density contrast should be achieved in a small region. An increase in the density contrast, e.g., from 100 to 1000, can significantly improve the strength, considering that the cloud crushing time scale is proportional to $t_{cc} \propto r_c^{-1/2}$ for a fixed mass (WC02, Klein et al. 1994). Such small-sized but dense clumps are likely to form, given the steep density profile of the shell.

In our model for Type Ia supernovae ($M = 1.4 M_\odot$, $E_{51} = 1$, and $M_{Ni} = 0.5 M_\odot$), the frozen-in velocity reaches $v_f \sim 7000 \text{ km s}^{-1}$, resulting in a clump-remnant interaction initiated in an early state, $t' \sim 1.02$. Compared to the present state $t' \sim 1.7$ of Tycho’s remnant, the ejection has a strength as indicated for Tycho’s knots in our previous 2-D HD simulations (WC01). In addition, the swept-up mass $\sim 0.5 M_\odot$ in the shell is reasonably in excess of the mass $0.002 M_\odot$ for the Si+S clump and $0.0004 M_\odot$ for the Fe clump in Tycho’s SE outline (Hwang, Hughes, & Petre 1998). However, there is evidence for Tycho that it is subluminous (van den Bergh 1993; Schaefer 1996), implying a deficiency in ^{56}Ni . Observations of SN 1006 suggest an initial Nickel mass in the range of $0.075 - 0.16 M_\odot$ (Hamilton et al. 1997, Mazzali et al. 1997). For Sn 1991 bg, Mazzali et al. (1997) estimate $0.07 M_\odot$ of ^{56}Ni extending to a velocity of $5,000 \text{ km s}^{-1}$. In our model, the velocity only extends to $\lesssim 4,000 \text{ km s}^{-1}$ with $M_{Ni} = 0.07 M_\odot$.

For core collapse supernovae, we consider that the object RX J0852–4622 superposed the boundary of the Vela remnant is a result of the clump-remnant interaction. WC02 estimated a mass of $0.1\beta M_\odot$, where $\beta < 1$, for the responsible clump, which gives a fraction $\lesssim 10\%$ in terms of the total swept-up mass in the shell. This mass fraction appears somewhat large compared to the Si+S clump in Tycho’s remnant. It is unclear how such a massive clump is created, if the initial ^{56}Ni is not overabundant.

In our scenario, the initial ^{56}Ni has a symmetric distribution in the center of supernova ejecta. It should be noted that dynamical processes prior to the Nickel bubble effect, e.g., neutrino-driven convection (Kifonidis et al. 2000), may give rise to an anisotropic distribution of elements. If ^{56}Ni is mixed outwards during the explosion, the amount of radioactive material inside each individual bubble could be orders of magnitude lower; the subsequent radioactive heating may cause merging between Nickel bubbles, and so give further compression. This process remains to be examined by future multidimensional calculations. Our result here should be noted as a lower limit on the ejecta-clump properties for the clump-remnant interaction.

6. CONCLUSIONS

We investigated the ejecta structure in supernovae due to the radioactive heating from the $^{56}\text{Ni} \rightarrow ^{56}\text{Co} \rightarrow ^{56}\text{Fe}$ decay sequence, under the assumption of spherically symmetric flow. Two approaches were used: hydrodynamics (HD) simulations and radiation hydrodynamics (RHD) simulations. The RHD calculation included a proper treatment of radiation transport prior to the age 10^7 sec, when about 25% of the total radioactive energy is still to be released. Radiative effect becomes dynamically less important as the evolution tends towards the optically thin regime. Based on the mutual coherence in the HD and RHD calculations, we obtained the properties of the shell driven by the radioactive expansion. We believe that going to later stages of diffusion would not change this conclusion.

The expansion of the Nickel bubble can sweep up a dense shell of $\lesssim 1 M_{\odot}$ shocked ambient ejecta in core collapse and Type Ia supernovae, with the highest density in the shell over 100 times the ambient ejecta density. The shell has an inward density increase toward the bubble-shell interface, and the highest density contrast computed is limited by numerical resolution. For the hydrodynamical solution, the structure of the shell can be approximately described by a self-similar solution. For the RHD solution, the main difference is that radiative diffusion gives rise to a broader and less dense shell that freezes out in the ejecta. Because the radioactive pressure eventually dominates, the saturated solution is not sensitive to the initial conditions such as the background pressure and the initial density contrast of Ni; the only crucial factor to the solution is the initial ^{56}Ni abundance. We presume that a higher background pressure due to the uncertainty of the adiabat would not affect the results.

We examined if the properties of the shell fragments are comparable to that of the ejecta clumps protruding the outlines of Tycho’s remnant and the Vela remnant. The density contrast created across the shell, $\chi \sim 100$, is compatible with that of the ejecta clumps needed to survive the clump-remnant interaction. In our standard Type Ia model, the shell’s frozen-in velocity attained at $\sim 10^6$ sec appears sufficient to give an ejection as indicated for Tycho’s knots, in spite that most ($\lesssim 75\%$) of the radioactive energy is still to be released. For core collapse supernovae like the Vela remnant, however, the small size and the late ejection of the inferred clump result in a weak strength to resist crushing and further cause protrusions on the remnant outline.

I am grateful to Roger Chevalier for supporting this work, and Toshi Shigeyama for useful correspondence on Type Ia supernovae. I thank the referee for careful and constructive comments on the manuscript. The computations were carried out on the IBM SP2 at University of Virginia, and the PC cluster provided by Taiwan’s NSC grant NSC93-2112-M033-002. Support for this work was also provided by NSC grant NSC93-2112-M033-013..

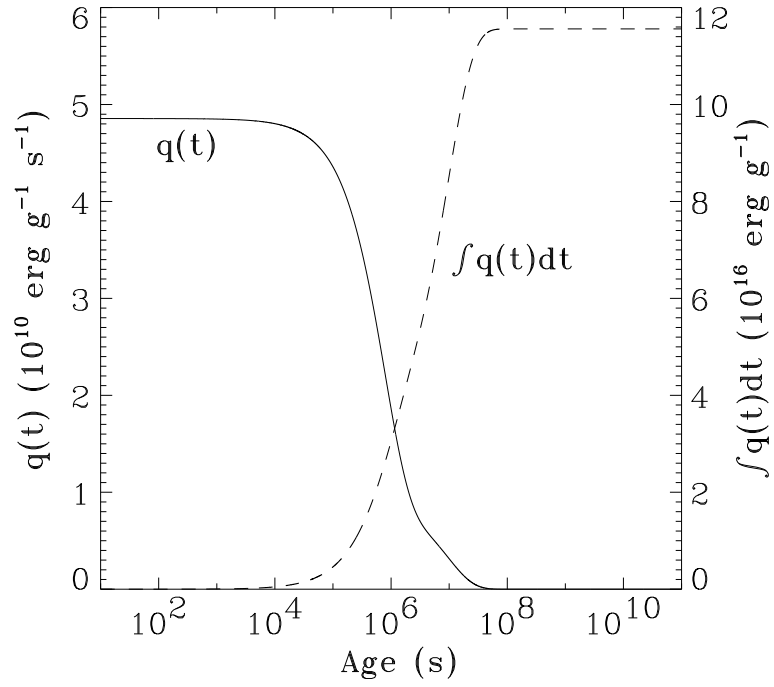


Fig. 1.— Evolution of the instantaneous and accumulated heating rate of the Nickel and Cobalt radioactive decay.

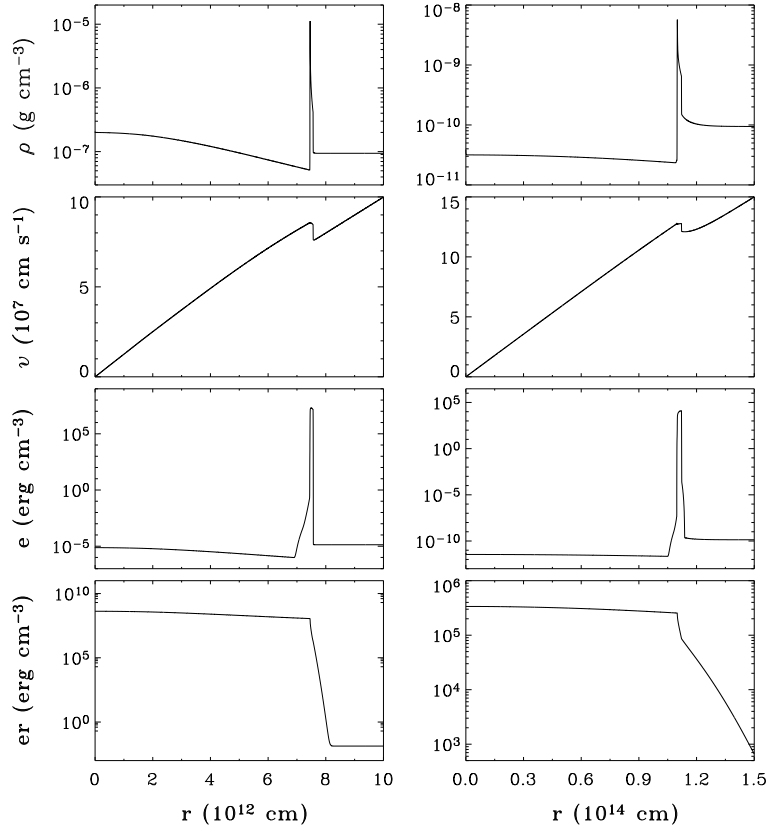


Fig. 2.— Distributions of density, velocity, gas energy density, and radiation energy density of the Nickel bubble structure in the flat-density ejecta of the core collapse supernova at 10^5 and 10^6 sec. The initial Nickel mass is $M_n = 0.075 M_\odot$. The grid has 8000 uniform zones that resolve the shell into ~ 100 zones.

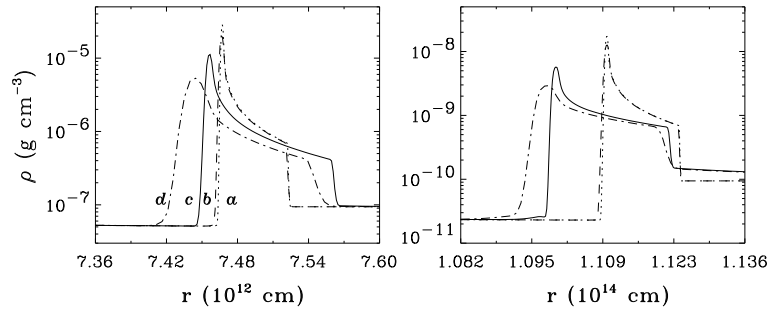


Fig. 3.— Density profiles of the Nickel bubble shell in the core collapse SN model at 10^5 and 10^6 sec. a: HD solution on a nonuniform grid of 8000 zones that resolves the shell into 200 zones. b: HD solution on a uniform grid of 8000 zones. c: RHD solution on a uniform grid of 8000 zones. d: RHD solution on a uniform grid of 2000 zones.

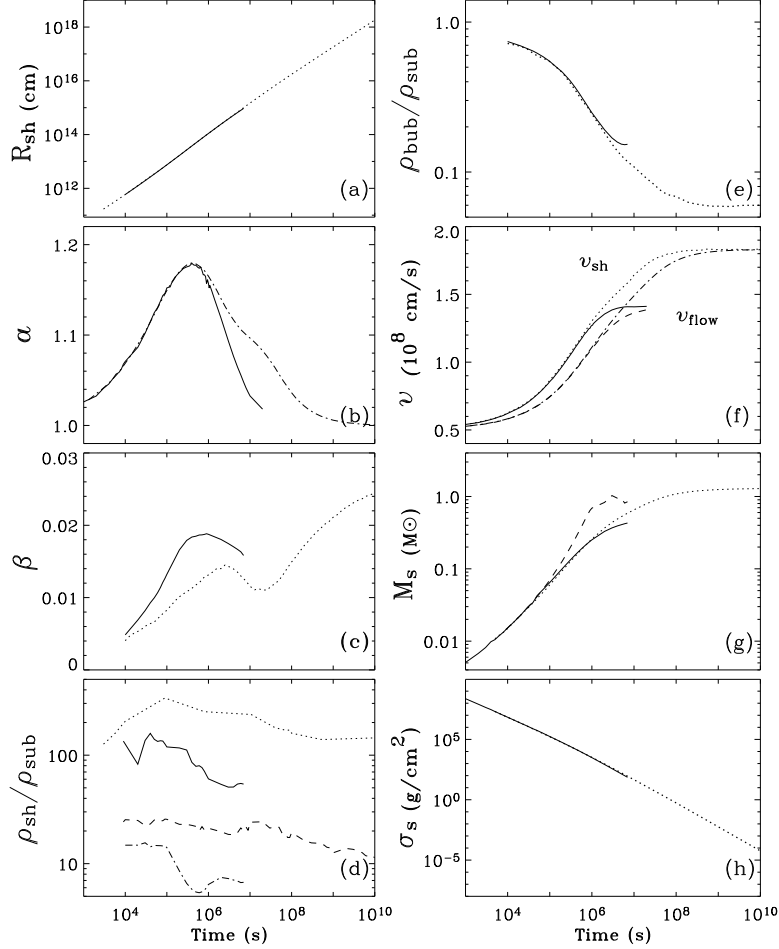


Fig. 4.— Evolution of the dynamical properties of the Nickel bubble shell in the core collapse SN model. Solid and dotted lines represent the RHD and the HD case, respectively. (a) Radius of the shock R_{sh} . (b) Expansion rate of the shell, $a = d \ln R_{sh} / d \ln t$, equivalent to the velocity contrast between the shock and the ambient free-expanding ejecta. (c) Thickness ratio β of the shell. The value is influenced by numerical resolution. (d) Density contrast between the densest region in the shell and the ejecta substrate. Dashed and dash dot lines represent the average density contrast in the HD and the RHD case, respectively. (e) Density contrast between the bubble and the ejecta substrate. (f) Shell velocity $v_{sh} = dR_{sh}/dt$ (left) and flow velocity $v_{flow} = R_{sh}/t$ (right) at the shock front. (g) Swept-up mass M_s in the shell. In the RHD case, two estimates are given for M_s due to the lower resolution. Solid line: estimated within the inner sharp edge of the shock front. Dashed line: estimated within the outer edge of the shock front where the density flattens out. (h) Surface density $\sigma_s \equiv M_s / 4\pi R_{sh}^2$ of the shell.

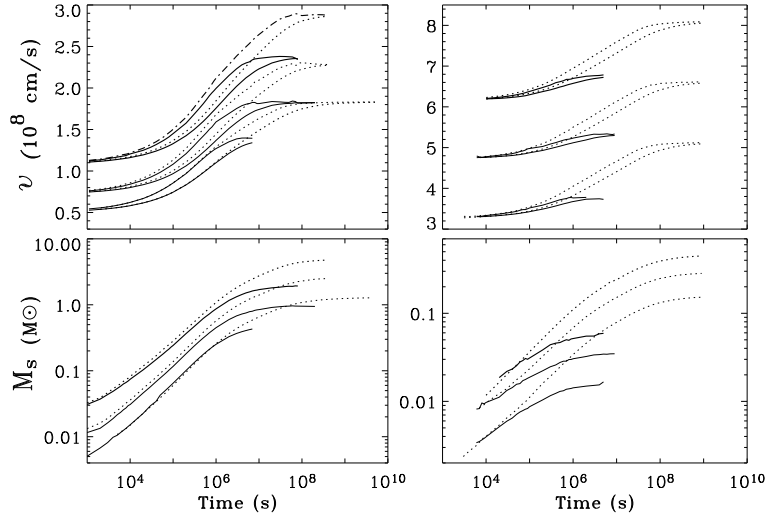


Fig. 5.— Evolution of shell and shock velocity and accumulated mass in the shell with varying initial Ni abundance. Solid and dotted lines represent the RHD and the HD case, respectively. Left: $M_{Ni} = 0.075$ (bottom line), 0.225 (middle line), and $0.75 M_{\odot}$ (top line) for the core collapse SN model. Right: $M_{Ni} = 0.075$ (bottom line), 0.225 , (middle line), and $0.5 M_{\odot}$ (top line) for the Type Ia SN model.

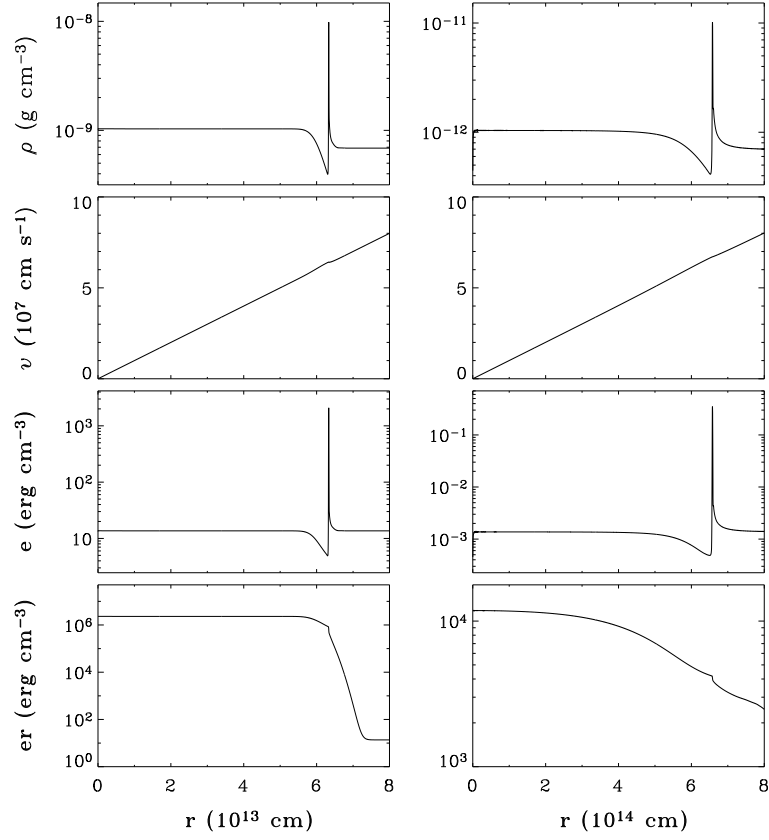


Fig. 6.— Distributions of density, velocity, gas energy density, and radiation energy density of the Nickel bubble structure in the Type Ia SN model at 10^5 and 10^6 sec. The initial Nickel mass is $M_n = 0.5 M_\odot$. The grid has 16000 uniform zones.

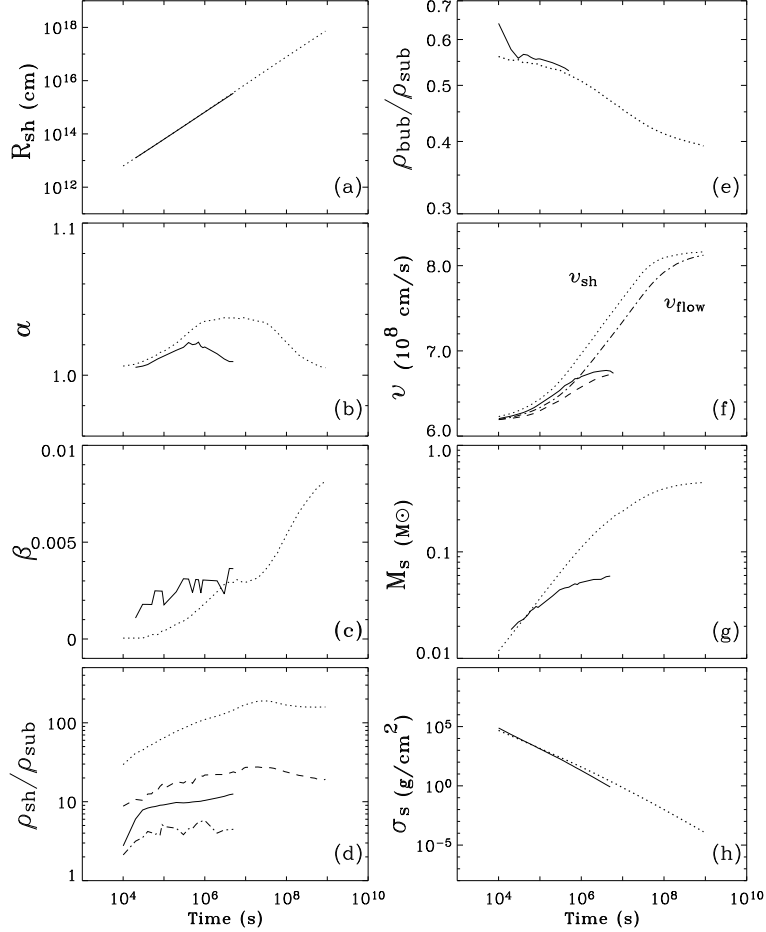


Fig. 7.— Evolution of the properties of the Nickel bubble shell in the Type Ia SN model. Solid and dotted lines represent the RHD and the HD case, respectively. (a) Radius of the shock R_{sh} . (b) Expansion rate of the shell, $a = d \ln R_{sh} / d \ln t$, equivalent to the velocity contrast between the shock and the ambient free-expanding ejecta. (c) Thickness ratio β of the shell. The thickness is estimated within the densest point and the outer edge of the shock front. In the RHD case it is not well defined due to a low resolution. (d) Density contrast between the densest region in the shell and the ejecta substrate. Dashed and dash dot lines represent the average density contrast in the HD and the RHD case, respectively. (e) Density contrast between the bubble and the ejecta substrate. (f) Shell velocity $v_{sh} = dR_{sh}/dt$ (left) and flow velocity $v_{flow} = R_{sh}/t$ (right) at the shock front. (g) Swept-up mass M_s in the shell. In the RHD case, M_s is estimated within the outer edge of the shock front without the precursor. (h) Surface density $\sigma_s \equiv M_s / 4\pi R_{sh}^2$ of the shell.

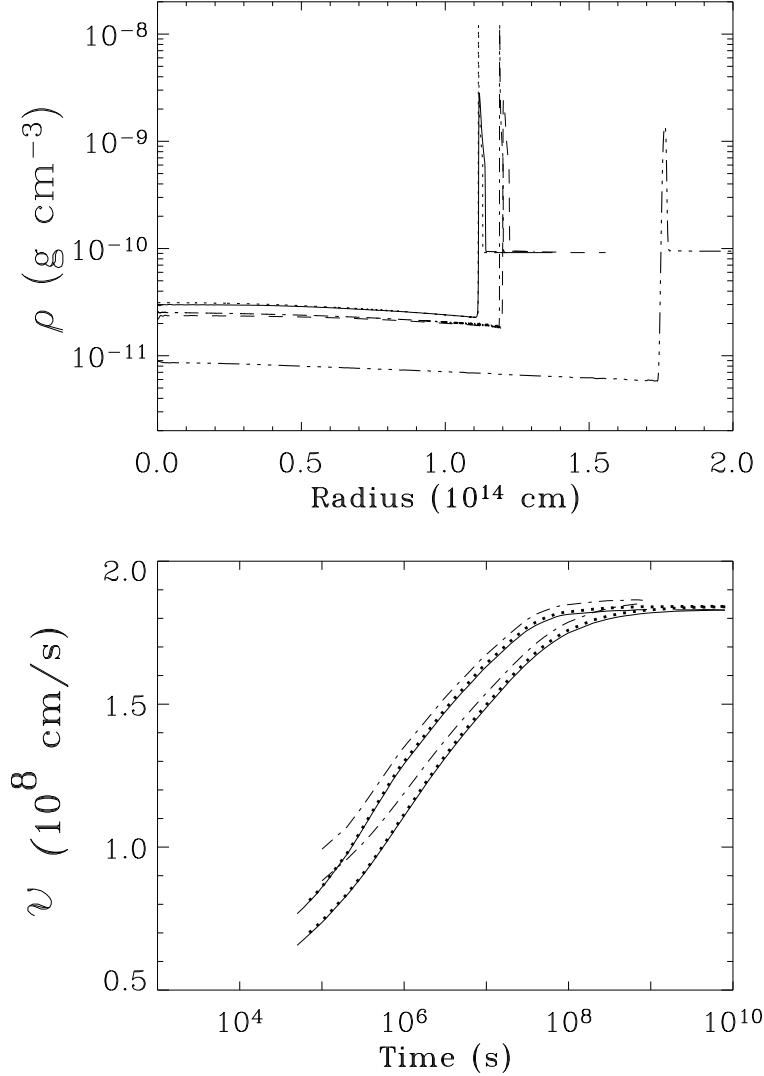


Fig. 8.— Density profiles at 10^6 sec (top) and evolution of shell and flow velocities (bottom) in HD models for core collapse SNe with varying initial parameters. The runs in dotted and dash dot lines use a resolution of 8000 zones, others use a resolution of 2000 zones. Solid line: $t_0 = 10^4$ sec, $e_0 = 2.7 \times 10^{11}$ (cgs units), and $\omega = 3$. Dotted line: $t_0 = 10^2$ sec, $e_0 = 2.7 \times 10^{18}$ (cgs units), and $\omega = 3$. Dashed line: $t_0 = 10^4$ sec, $e_0 = 2.7 \times 10^{11}$ (cgs units), and $\omega = 1$. Dash dot: $t_0 = 10^2$ sec, $e_0 = 2.7 \times 10^{18}$ (cgs units), and $\omega = 1$. Dash dot dot dot: $t_0 = 10^2$ sec, $e_0 = 2.7 \times 10^{18}$ (cgs units), and $\omega = 0.1$.

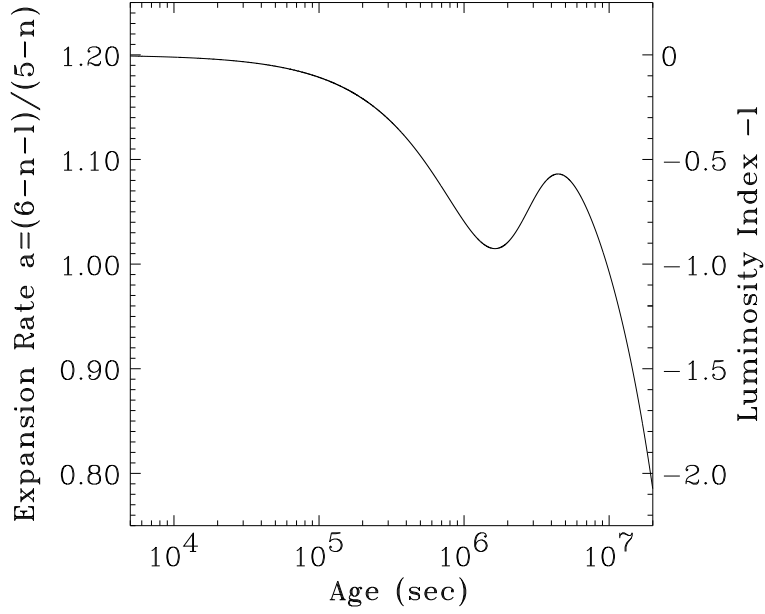


Fig. 9.— Luminosity index l of Nickel radioactivity and expansion rate a derived from the self-similar solution, $a = (6 - n - l)/(5 - n)$.

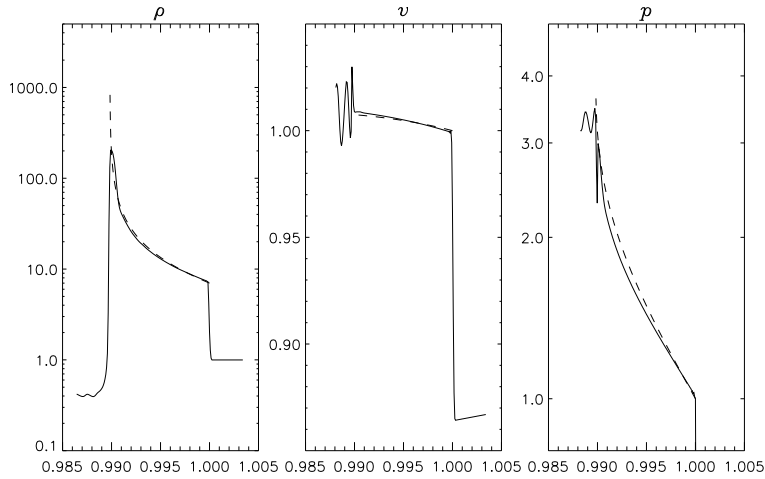


Fig. 10.— Hydrodynamical solutions of the Nickel bubble shell in the core collapse SN model at 4.0×10^5 sec overplotted on the self-similar solutions of $\gamma = 4/3$, $n = 0$, $l = 0.3$, and $a = 1.14$. The velocity and pressure show large post shock oscillations behind the contact discontinuity.

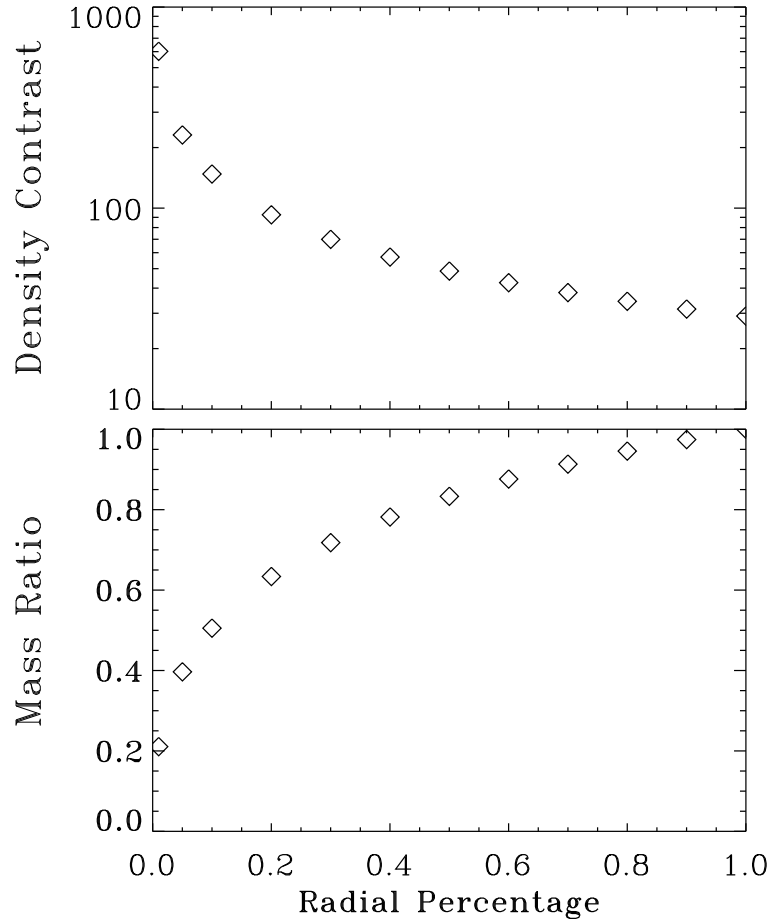


Fig. 11.— Top: Density contrast of the self-similar solution at 4×10^5 sec integrated over a radial fraction of the shell from the contact discontinuity. The innermost 1% region of the shell has an average density contrast over 600, while the total average is 20. Bottom: Integrated mass distribution.

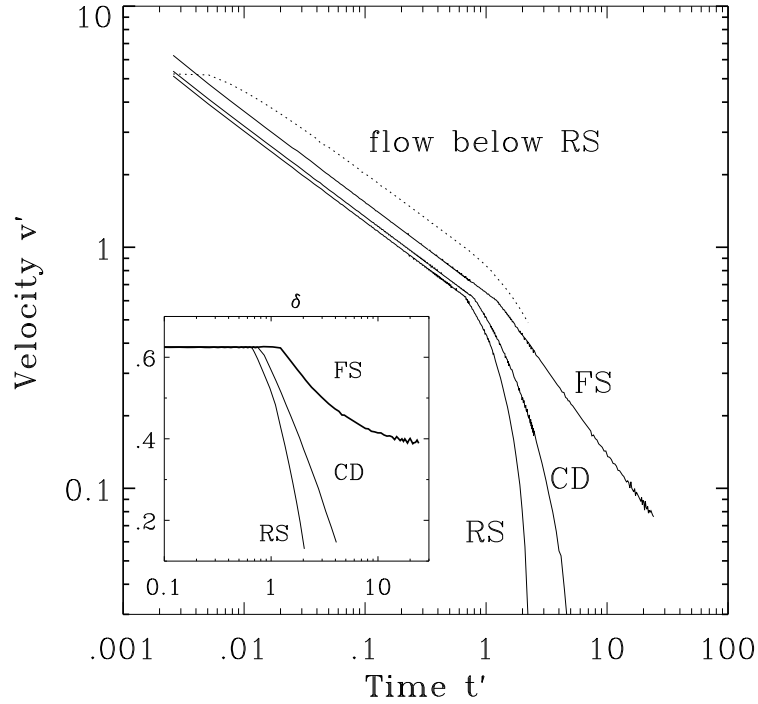


Fig. 12.— Evolution of velocities in a supernova remnant with $n=8$ ejecta and a constant density ambient medium as described in WC02. Dotted line: flow velocity of the ejecta immediately below the reverse shock (RS). Solid lines: the pattern velocities and deceleration parameters $\delta = d \ln r / d \ln t$ (inset) of the forward shock (FS), the contact discontinuity (CD), and the reverse shock with time. The quantities v' and t' are normalized to scaling parameters given in WC 02. In our model for core collapse supernovae, $v = 3162 v'$ (km/s) and $t = 1271 t'$ (yr); for Type Ia supernovae, $v = 8452 v'$ (km/s) and $t = 244 t'$ (yr).

REFERENCES

- Audi, G., Wapstra, A. H., & Thibault, C. 2003, Nucl. Phys. A729, 337
(<http://ie.lbl.gov/toimass.html> for the atomic mass)
- Aschenbach, B., Egger, R., & Trümper, J. 1995, Nature, 373, 587
- Basko, M. 1994, ApJ, 425, 264
- Chevalier, R. A. 1976, ApJ, 207, 872
- Chevalier, R. A. 1984, ApJ, 280, 797
- Chevalier, R. A., & Liang, E. P. 1989, ApJ, 344, 332
- Dwarkadas, V., & Chevalier, R. A. 1998, ApJ, 497, 810
- Fireston, R. B., & Shirley, V. S., ed 1996, Table of Isotopes (8th ed.; John Wiley & Sons, Inc.)
- Lide, D. R., ed 1992, CRC Handbook of Chemistry and Physics (73d ed.; Boca Ration: CRC Press), 11-38
- Filippenko, A. V., & Sargent, W. L. W. 1989, ApJ, 345, L43
- Hamilton, A. J. S., Fesen, R. A., Wu, C.-C., Crenshaw, D. M., & Sarazin, C. L. 1997, ApJ, 482, 838
- Hwang, U., Hughes, J. P., & Petre, R. 1998, ApJ, 497,833
- Jun, B.-I. 1998, ApJ, 499, 282
- Kifonidis, K., Plewa T., Janka, H.-Th, & Müller, E. 2000, ApJ, 531, L123
- Klein, R. I., McKee, C. F., & Colella, P. 1994, ApJ, 420, 213
- Li, H., McCray, R., & Sunyaev, R. A. 1993, ApJ, 419, 824
- Lide, D. R., ed 1992, CRC Handbook of Chemistry and Physics (73d ed.; Boca Ration: CRC Press), 11-38
- Matheson, T., Filippenko, A. V., Ho, L. C., Barth, A. J., & Leonard, D. C. 2000, AJ, 120, 1499
- Mazzali, P. A., Chugai, N., Turatto, M., Lucy, L. B., Danziger, I. J., Cappellaro, E., Della Valle M., & Benetti, S. 1997, MNRAS, 284, 151

- McCray, 1993 ApJ, 510, 379
- Nomoto, K., Thielemann, F.-K., & Yokoi, K. 1984, ApJ, 286, 644
- Reynoso, E. M., Vel'azquez, P. F., Dubner, G. M., & Goss, W. M. 1999, AJ, 117, 1827.
- Schaefer, B. E. 1996, ApJ, 459, 438
- Shigeyama, T., & Nomoto, K. 1990, ApJ, 360, 242
- Spyromilio, J. 1994, MNRAS, 266, L61
- Stathakis, R. A., Dopita, M. A., Cannon, R. D., & Sadler, E. M. 1991, in *Supernovae*, ed. S. E. Woosley (New York: Springer) 95
- Stone, J. M., Mihalas, D., & Norman, M. L. 1992, ApJS, 80, 819
- van den Bergh, S. 1993, ApJ, 413, 67
- Wang, C.-Y., & Chevalier, R. A. 2001, ApJ, 549, 1119 (WC01)
- Wang, C.-Y., & Chevalier, R. A. 2002, ApJ, 574, 155 (WC02)
- Winkler, P. F., Tuttle, J. H., Kirshner, R. P., & Irwin, M. J. 1988, in *Supernova Remnants and the Interstellar Medium*, ed. R. S. Roger & T. L. Landecker (Cambridge: Cambridge Univ. Press), 65
- Woosley, S. E. 1988, ApJ, 330, 218
- Woosley, S. E., Pinto, P. A., & Hartmann, D. 1989, ApJ, 346, 395